An artificial nervous system for communication between wearable and implantable therapeutics

Ramy Ghanim[1,#], Yoon Jae Lee[2,3,#], Garan Byun[2,4], Joy Jackson[5], Julia Z. Ding[5], Elaine Feller[1], Eugene Kim[2,6], Dilay Aygun[1], Anika Kaushik[1], Alaz Cig[6], Jihoon Park[1], Sean Healy[5], Camille E. Cunin[7], Aristide Gumyusenge[7], Woon Hong Yeo[2,4,5,6,*], Alex Abramson[1,2,5,8,*]

[1]School of Chemical and Biomolecular Engineering, Georgia Institute of Technology, Atlanta, GA 30332, USA

[2]Wearable Intelligent Systems and Healthcare Center (WISH Center), Institute for Matter and Systems, Georgia Institute of Technology, Atlanta, Georgia 30332, USA

[3]School of Electrical and Computer Engineering, Georgia Institute of Technology, Atlanta, Georgia 30332, USA

[4]Parker H. Petit Institute for Bioengineering and Biosciences, Institute for Robotics and Intelligent Machines, Georgia Institute of Technology, Atlanta, GA 30332, USA

[5]The Wallace. H. Coulter Department of Biomedical Engineering, Georgia Institute of Technology, Atlanta, GA 30332, USA

[6]George W. Woodruff School of Mechanical Engineering, Georgia Institute of Technology, Atlanta, GA 30332, USA

[7]Department of Materials Science and Engineering, Massachusetts Institute of Technology, Cambridge, MA 02139, USA

[8]Division of Digestive Diseases, Emory University School of Medicine, Atlanta, GA 30322, USA

[#]Co-First Author

*Correspondence to: aabramson6@gatech.edu, whyeo@gatech.edu

Abstract

Bioelectronics have transformed our capacity to monitor and treat diseases; however, a lack of micrometer-scale, energy efficient communication options limit these devices from forming integrated networks that enable full-body, sensor driven, physiological control. Inspired by our nervous system's ability to transmit information via ionic conduction, we engineered a Smart Wireless Artificial Nervous System (SWANS) that utilizes the body's own tissue to transmit signals between wearables and implantables. When SWANS emits signals, it generates voltage gradients throughout the body that selectively turn on implanted transistor switches when exceeding their gate threshold voltages. SWANS' implantable communication components maintain syringe-injectable footprints and >15x greater power efficiencies than Bluetooth and Near Field Communication. In vivo studies in rats demonstrate SWANS' ability to wirelessly regulate dual hind leg motor control by connecting electronic-skin sensors to implantable neural interfaces via ionic signaling as well as coordinate bioelectronics throughout the epidermal, subcutaneous, intraperitoneal, and gastrointestinal spaces.

Introduction:

Wearable [1, 2], implantable [3-6], and ingestible [7, 8] bioelectronics monitor and treat the world's most prevalent illnesses including diabetes [9, 10], cancer [11, 12], and heart disease [13, 14]; however, almost all bioelectronics work independently from one another, limiting the capacity for biosensors to interact and remotely trigger therapeutics. In-body networks of electronic therapeutics are inherently limited by the large power and size requirements necessary for communication that limit implant battery lifetimes to weeks and necessitate invasive surgical implantation [15-17]. One example of sensors and therapeutics working side-by-side is the wearable continuous glucose monitor and insulin pump; yet insulin pumps' batteries, measuring 8 cm^3, only last 7 days partially due to constant Bluetooth Low Energy (BLE) connectivity [18]. Other wireless communication and power transfer methods, such as near-field communication (NFC), require bulky external antennae that limit patient adherence and require centimeter-scale alignment with targeted devices [19, 20]. Here, we harness the conductive nature of body tissue to transmit communication signals ionically between wearable sensors and implantable devices. In the process, we create an artificial nervous system that: (1) reduces communication components to an emitted square-wave pulse and a single micrometer-scale transistor per implanted device; (2) independently triggers multiple devices throughout the tissue from a multiplexed wearable hub; and (3) extends the battery life of implanted devices compared to NFC and Bluetooth by 15x and 30x, respectively.

Here, we introduce SWANS, the Smart Wearable Artificial Nervous System. SWANS unlocks the potential for long-term closed-loop networks of wearable and in-body therapeutics by providing a framework for communication between dispersed bioelectronics via intertissue ionic conduction **(Fig. 1A)**. To enable effective communication, SWANS' wearable biosensor hub emits electrical

pulses that produce electric fields inside the body; then, the implantable receiving network detects the generated voltage gradient through tissue-interfacing pads to turn on a transistor switch which briefly enables a therapeutic action **(Fig. 1B)**. Each implant possesses a unique transistor circuit that only responds to its corresponding signal. The U.S. Food and Drug Administration has already confirmed the safety and efficacy of in-body ionic communication in humans for other uses [21]; for example, Abilify MyCite pills utilize ionic conduction to transmit ingestion event data from an oral drug tablet to a wearable device by recording the presence or absence of an electrical signal in the body [22, 23]. Preclinical studies have also utilized ionic conductance to similarly transmit data across tissues from implantable [24], wearable [25], and ingestible [26] sensors. Additionally, engineers have previously attempted to create body-networks of wearable sensors without including implants [27, 28]; however, a fully functional body-therapeutic-network requires integration of both sensors and actuators across all tissue depths to enable closed-loop therapies. We demonstrate in vivo in rats that SWANS can wirelessly trigger subcutaneously implanted, intraperitoneally implanted, and gastrointestinally localized actuators via sensors and electronics placed on the epidermis. Furthermore, we demonstrate in vivo proof-of-concept by utilizing the SWANS architecture to wirelessly trigger implantable sciatic nerve stimulators for dual hind-leg animation. By detecting front limb motion and activating hind leg motion, we show that SWANS mimics how nervous systems selectively trigger and transmit targeted signals from one end of the body to another.

In-Body ionic communication for triggering bioelectronic therapeutics

SWANS shrinks the size of implanted communication components **(Fig. 1C-D)** and improves the battery life of implantable devices compared to those employing BLE and NFC communication by utilizing micrometer-scale, low-power transistor switches to regulate DC output and on/off states; this compares to BLE system on a chip components that measure at least 6 mm in width and NFC antennas that can reach centimeter scale in size. SWANS ensures that the current through the device remain essentially zero unless the transistor enters the active or saturation regions. For example, a neurostimulator powered by a 1.55 V coin cell battery consumes 0.14 ± 0.02 mWh, 2.1 ± 0.3 mWh, and 4.1 ± 1.4 mWh (n = 3, Avg ± SD) when triggered via SWANS, NFC, and BLE, respectively **(Fig. 1E, Supplementary Fig. S1).** While BLE device lifetimes can be improved by decreasing the passive current draw used for advertisement procedures [29], this approach effectively limits the feasibility of integrating devices into rapid-acting closed loop systems. In contrast, the SWANS communication structure allows for compact devices with round-the-clock connectivity and effectively no passive current draw.

Each SWANS implant possesses two tissue-interfacing receiving pads connected to the gate pins of a transistor that detect emitted voltage gradient signals in the tissue and facilitate switching. By utilizing different types of transistors switches and passive circuit components, each SWANS implant responds only to a characteristic pulse magnitude, width, and frequency emitted by the wearable hub, enabling the hub to control implants individually. For example, an NPN bipolar junction transistor (BJT) switches on when the potential difference between the base and emitter approaches 0.7 V. Conversely, a PNP BJT turns on around 0.1 V and off near 0.7 V. An N-channel enhancement mode MOSFET transistor turns on at a prescribed threshold voltage, typically from 0.5 V to ≥ 2.0 V. Alternatively, organic electrochemical transistors (OECTs) respond to increasing

triggering pulse lengths and rising numbers of sequentially applied pulses by remaining in their on states for proportionally longer periods of time. Additionally, by adding a resistor in between the harvesting pad and the transistor gate of an NPN transistor, it is possible to further increase the required applied voltage gradient necessary for switching. Similarly, by adding a capacitor between the base and emitter of an NPN transistor, it is possible to increase the required pulse length necessary to switch on the implant. With distinct switching criteria for each implanted transistor switch circuit, it is possible to selectively or additively trigger actuation events by applying different voltage gradients to the tissue via wearable source and ground probes.

We engineered the SWANS system to selectively communicate with multiple implanted devices placed anywhere within the body's conductive tissue by optimizing the voltage magnitude applied to the tissue by a wearable hub as well as the separation distance and surface area of implanted pads used to receive the in-body voltage gradient. In ex vivo studies on chicken breast tissue, the potential difference between receiving pads scaled linearly with the voltage applied by the wearable signal injection probes **(Fig. 1F)**. Applications of 1V, 2V, and 4V pulses yielded received voltage gradients by the implanted pads of 0.20 ± 0.04 V, 0.40 ± 0.06 V, and 0.75 ± 0.07 V (n = 10, Avg ± SD). These pulses provided voltage gradient magnitudes with sufficiently small errors to uniquely regulate the activity of 2N2907 PNP, P55NF06L MOSFET, and 2N2222 NPN transistors, respectively. Increasing the resistance between an NPN base and harvesting pad increased the pulse voltage magnitudes necessary for switching by up to 30% (n=10, **Fig. 1 G**). Adding a capacitor between the NPN base and emitter increased the required pulse lengths necessary for switching from 20 μs to 50-3000μs (n=6-11, **Fig. 1 H**). Combining these two findings, we demonstrated that long pulses with low voltage magnitudes (3.3 V, 2 ms) triggered switches that possessed an added 1 μF capacitor while short pulses with high voltage magnitudes

(4 V, 0.05 ms), triggered switches with an added 2.2 kΩ resistor. The pulses that turned on one switch did not turn on the other switch, demonstrating the capacity to uniquely trigger implants (n=8**, Fig. 1 I**). In the case of OECTs, we demonstrated unique triggering patterns in the ex vivo SWANS setup compared to other tested transistors, modulating their switching times based on pulse length and frequency **(Supplementary Fig. S2)**.

The implanted SWANS receiving pads successfully trigger transistor switches when placed across a wide range of orientations, angles, and locations in the tissue. This occurs because the tissue's conductivity spreads the voltage gradient throughout the entire body. **Fig. 1J** provides a heat map of voltage measurements within an ex vivo chicken breast following an application of a 6V, 1Hz, 200 µs pulse. The relative orientation of the implanted receiving pads compared to the wearable signal injection probes moderately affects the magnitude of the received voltage gradient. However, this experiment demonstrated the possibility of receiving a > 1 V gradient anywhere between the signal injection and grounding pads, even at angles and locations that are not directly aligned between the two signal transmitter probes.

Ionic communication can trigger millimeter-scale SWANS implants at varying distances and depths away from the wearable signal injection hub. Ex vivo chicken breast studies confirmed that receiving pad separation distances of just 5 mm are sufficient to trigger transistor switches (total communication component size 7 mm x 1 mm), and the required distance between these pads scales with the distance from the signal injection probes (**Supplementary Fig. S3**). Multiple transistors can be uniquely triggered at distances and depths of up to 4 cm away from the signal injection probe (n = 10, **Fig. 1K**); for context, the average skin and subcutaneous fat tissue thickness in a human measures 1.2 ± 0.6 cm [30]. While further increasing the distance reduces the ability to selectively trigger the implants, all three transistors can be triggered with reduced

fidelity at distances and depths of up to 6 cm away from the signal injection probe. Additionally, changing the surface area of the conductive receiving pads between 1-300mm^2 provided negligible improvement in voltage gradient reception, allowing us to minimize the size of the implanted receiving pads (**Supplementary Fig. S3**). COMSOL simulations provided additional data regarding the effects of pad orientations and separations on electric field generation in both rat- and human- sized tissue models, suggesting that larger distances could be covered by ionic communication in larger models (**Supplementary Fig. S4**). Having determined minimum pad separation lengths, sizes, and orientations for triggering implanted transistors, we next designed wearable and implantable circuits for in vivo SWANS applications.

A platform for low-power, wireless communication between wearables and implantables

The full in vivo SWANS architecture possesses three key components: (1) a central, wearable hub that coordinates sensor readouts and therapeutic actuation via in-body ionic communication; (2) a microneedle patch that interfaces between the wearable and the body; and (3) an implantable circuit that receives a unique signal and performs a therapeutic action (**Fig. 2A-B, Supplementary Fig. 5**). To enable sensor-guided signaling in vivo, we engineered a wearable flexible printed circuit board (fPCB) containing interchangeable physical or chemical sensors, a control unit, and a configurable voltage output capable of delivering up to 12 V (**Fig. 2C**). These signals are introduced into the tissue via stainless steel microneedle patches, bypassing the highly resistive stratum corneum and directly generating a voltage gradient beneath the skin (**Fig. 2D**). Previous animal and human studies on microneedles and electrical stimulation systems suggest that our employed microneedle lengths and applied current densities will provide a painless, safe, and straightforward user experience [31-35]. The resulting voltage gradient is then received by a custom-engineered, programmable, implantable fPCB containing two receiving pads, an interchangeable transistor switch, a power source, and an actuator such as a neurostimulator (**Fig. 2E**). In this way, SWANS effectively operates as a low-power, end-to-end communication platform, wirelessly linking wearable sensors to in-body therapeutics.

The SWANS wearable hub receives inputs from multiple sensors, processes this data, and transmits ionic-communication pulses from 0 V – 12 V into the tissue to control implantable bioelectronics. In our proof-of-concept example, we place two laser-induced graphene (LIG)-based resistive strain sensors (**Supplementary Fig. S6**) on the forelimbs of rats to detect motion intent. The wearable Hub detects when the sensor signal surpasses a given threshold (**Fig. 2F**) and introduces a unique signal into the body depending on the limb that moved. Two implantables with unique transistor

switches are placed distally on each hind limb. When an implantable receives its corresponding signal, it stimulates the sciatic nerve on the specified hind leg. Thus, SWANS possesses full control over multiple bioelectronic implants. The implantable circuit's architecture enables control over a wide array of therapeutically relevant devices in addition to neural interfaces such as pumps and micro-LEDs (**Supplementary Fig. S7**).

The size of the implantable is dictated by the receiving pad separation distance required to trigger transistors at a given depth and the battery requirements for the actuating component. A 2.5 cm pad separation allows for independent control over the three transistors of interest when placed up to 4 cm deep in the tissue; notably, however, the communication components of the device can be scaled down to 7 mm^2 (7 mm x 1 mm) and still enable switching. This allows for the communication system to fit entirely within a 16 gauge needle and makes it over 5x smaller than the nRF52832 BLE system on chip (6 mm x 6 mm) as well as 1-2 orders of magnitude smaller than many NFC tags [36, 37], where working distance scales with coil length.

Due to the highly resistive nature of the stratum corneum, we implemented stainless steel microneedles into the wearable to enable direct electric field generation in the subdermal space, thereby increasing the relative voltage gradient inside the tissue. Microneedles at least 250 μm in height decrease the tissue-electrode interfacial impedance by 4x and increase generated subdermal voltage gradients **(Fig. 2G-H)**.

In vivo ionic communication patterns in rats resembled the trends found during ex vivo chicken breast studies **(Fig. 3A-C)**. Received voltage gradients scaled according to the applied signal and diminished in proportion to the distance between wearable and implanted modules. Application of 7.5 V pulses by a wearable SWANS signal injection probe led to an average received voltage of 0.87 ± 0.16 V, enough to switch an NPN transistor in the subcutaneous space into its active regions

during 26/27 trials **(Fig. 3A)**. All PNP and MOSFET transistors actuated in the subcutaneous space at lower signal injection voltages. In the intraperitoneal space, a MOSFET implant entered its active region 9/9 times at an application of 7.5 V, but an NPN transistor only actuated during 6/9 trials **(Fig 3B)**. Receiving pads in the stomach enabled PNP transistor switching at applied voltages of 7.5 V, indicating a possibility for gastrointestinal resident electronics to be regulated via SWANS **(Fig. 3C)**.

In vivo experiments in rat models demonstrated that SWANS implants successfully actuate when placed at varying orientations, locations, and depths within the tissue. We observed sufficient voltage gradients to trigger a transistor regardless of the spatial orientations of the V_{in} and ground microneedles, including placements horizontally, diagonally, and vertically across the flanks of the rats **(Fig. 3D)**. While the voltage gradient is maximized when TX-RX modules are superposed on each other, as ohmic losses are minimized in this case, current spreads in all directions from the V_{in} source creating voltage gradients in distant areas such as the gastrointestinal tract and the opposite flank of the rat.

Hematoxylin and Eosin as well as Masson's Trichrome histology staining provided evidence that SWANS 1 Hz pulses of voltages ≤ 10 V for lengths ≤ 10 ms did not generate cellular or tissue damage. We collected rat skin samples after applying microneedles and electrostimulation to the same skin location for at least 100 pulses over the course of one week **(Fig. 3E)**. Previous work on electrical stimulation safety in humans and animal models suggest that the current, pulse length, voltage gradient, charge per phase, and charge density per phase applied by SWANS do not generate skin, neuron, or muscle tissue damage [32-34]. In our experiment, low current electrostimulation (≤ 5 mA, ≤ 10 V, ≤ 10 ms) induced no visual damage to cells around the microneedle patch and no signs of inflammation. As a positive control comparator, we applied 10

V gradients over 100 ms pulses for 2 hours to generate tissue damage and compare to our test samples.

To demonstrate SWANS' ability to wirelessly transmit targeted, therapeutically relevant signals across the body, we engineered a bilateral triggerable neurostimulator for rats. SWANS allowed for independent control over multiple implanted devices placed throughout the body in rats. LIG sensors placed on each front paw detected forelimb motion and transmitted this information to a wearable hub which recorded sensor data. When the hub determined that a signal from a given sensor channel exceeded background noise, it activated its voltage booster sending a voltage gradient through the body to trigger the implantable device. **(Fig. 4A**). We confirmed that both NPN and PNP transistor switches on separate implants could be sequentially triggered to deliver sciatic nerve stimulation via our sensor driven wearable hub (n=30 trials over 3 rats **Fig. 4 B-D**). In this setup, both NPN and PNP switches triggered leg motion at the higher voltage pulses while only the PNP turned on at the lower pulses. Following the left leg sensor reaching a given threshold, NPN switches turned on with large applied voltage pulses from our wearable device (5+ V), and following the right leg sensor reaching a given threshold, PNP switches turned on with smaller applied voltage pulses (2+ V). Implant activation allowed a sciatic nerve interfacing cuff to receive an influx of power to trigger hind leg motion in the respective limb where the triggered implant was located. As controls, we recorded that the wearable pulse alone without the implant had no impact on hind leg motion at either pulse magnitude, and that the devices alone without an applied pulse had no impact on hind leg motion either (n=30 trials over 3 rats). We captured wearable and implantable electrical data via an oscilloscope, associated sensor data via Bluetooth communication with a nearby tablet, and leg motion data via high speed video. We also created two implants that triggered independently of each other by adding a resistor between the havesting

pad and the base of one NPN implant and adding a capacitor between the base and emitter of a second NPN implant (**Fig. 4E** n=30 trials over 3 different rats). Due to tissue impedance variability between rats, these implants and pulses required individualized settings to ensure independent actuation. Only the capacitor (47-68 pF) implant stimuated leg motion during long pulses with medium voltages (1-2 ms, 3.2-8.1 V), and only the resistor implant (422-825Ω) stimulated leg motion during a shorter pulse with higher voltages (0.15-0.25 ms, 4.1-10 V). By forming a bio-integrated network of dispersed wearable and implantable sensors and actuators, the SWANS communication protocol provides a platform technology to enable full-body coordinated control over bioelectronic therapeutic networks.

Conclusions and Future Work

SWANS reads out wearable sensor data and wirelessly triggers networks of implantable therapeutic devices via ionic conduction. Here, we demonstrate sensor-mediated neuromodulation in rats, and our data suggests that future SWANS iterations could potentially restore limb locomotion [38, 39], actuate smart pills [40, 41], trigger drug delivery reservoirs [16, 17, 42], switch on optogenetic probes [43, 44], and modulate living cellular implants [45-47] as well as control other bioelectronics throughout the epidermal, subcutaneous, intraperitoneal and gastrointestinal spaces. SWANS implantables require an order of magnitude less power than BLE and NFC without necessitating an external antenna. SWANS excels in applications where infrequent triggering and low data transmission rates are required, as implants draw near-zero power consumption but have limited data transfer rates. The communication components alone can be scaled down to fit inside of a 16 gauge needle, are over 5x smaller than the nRF52832 BLE system on chip, and are orders of magnitude smaller than many NFC coils used in vivo [36, 37], opening a new sandbox for biomedical engineers. In the future, it may be possible to increase the complexity of data transmission to more than on/off signaling by adding a microcontroller that reads out pulsed patterns, but this will come at the cost of reduced battery life and increased size.

While preliminary histology studies suggest that SWANS current injections do not generate tissue damage, long-term pain measurement and tissue health studies in humans are required to determine the safety of the SWANS system. Future studies in large animal models will quantify generated voltage gradients over larger decimeter-scale distances, with previous studies in humans and large animals suggesting the scalability of ionic communication [23, 26]. Additionally, utilizing conductive gels on the skin may reduce the impedance across the stratum corneum, potentially eliminating the need for microneedles in cases that require lower voltage gradients [48]. The

communication efficacy achieved with this platform technology suggests that SWANS could support a new generation of dispersed and coordinated bioelectronic therapies, opening the possibility to integrate and network the countless numbers of wearable sensors and therapeutic devices being engineered for personalized medical treatments.

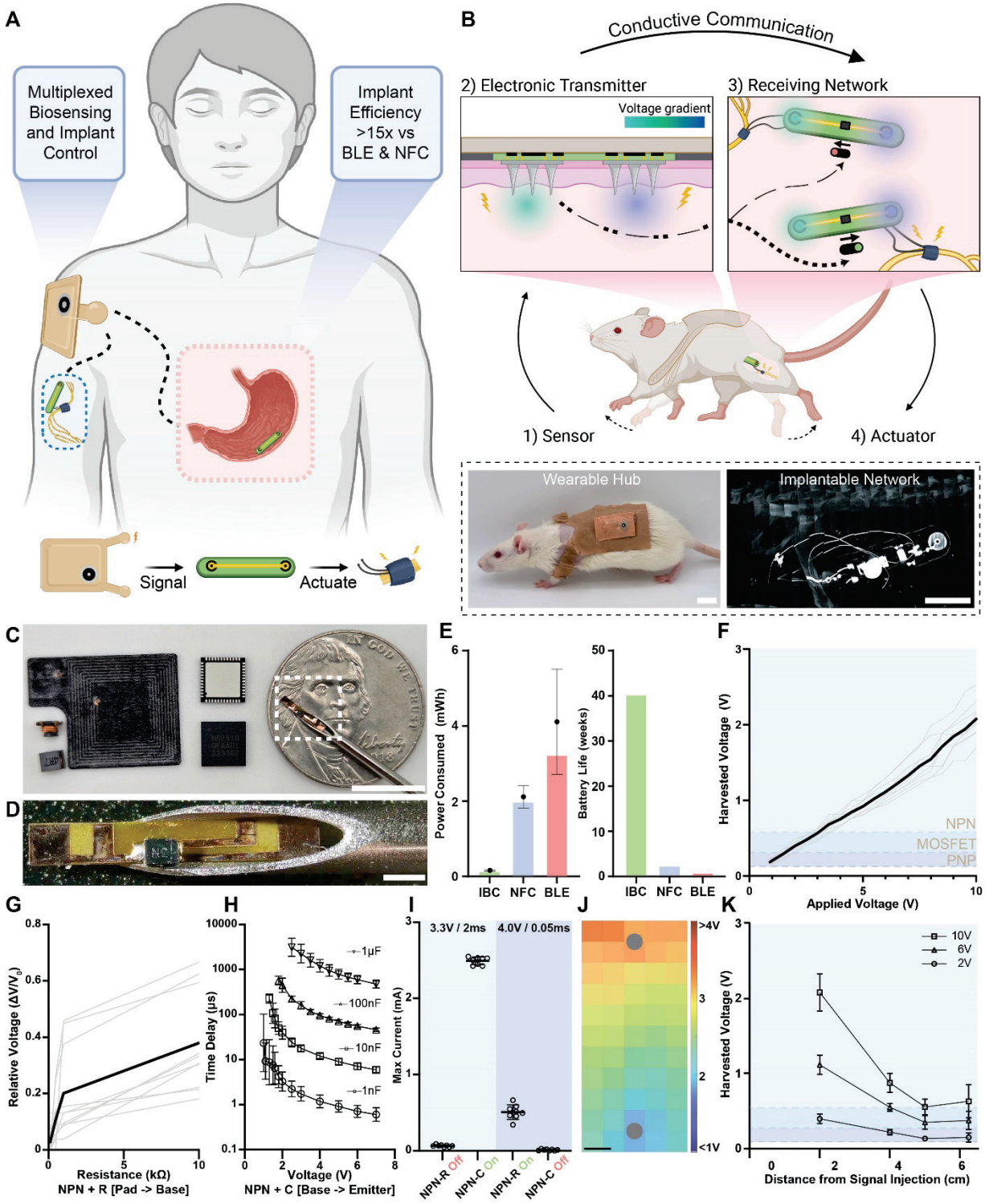

Fig. 1. In-body communication enables low-power networks of wearable and implantable therapeutics. (A) A smart wireless artificial nervous system [SWANS] utilizes a wearable hub to

control multiple therapeutic actuators throughout the subcutaneous, intraperitoneal, and gastrointestinal spaces by sending electrical signals ionically through tissue. **(B)** An example SWANS use case, where wearable sensors detect front limb motion, triggering a wearable hub to generate an electric field throughout the body. Distal implants receive the voltage gradient using tissue interfacing pads and turn on corresponding transistor switches. If the signals match, sciatic nerve stimulators are actuated for hind leg motor control. **(C)** Right to left: SWANS communication component; Bluetooth System-on-chip; millimeter-scale and centimeter-scale working distance NFC antennas. **(D)** Zoomed in SWANS communication component in 16-gauge needle. **(E)** Theoretical (bars) and experimental (points, Avg ± SD, n=3) power characteristics of implanted neuromodulation bioelectronics controlled via in-body ionic communication (IBC), Near Field Communication (NFC), and Bluetooth Low Energy (BLE). **(F)** Voltage measured across a transistor's gate when applying increasing amplitude pulses across ex vivo chicken breast tissue. Shaded regions denote transistor gate and threshold voltages. (black = avg, grey = ind; n = 9) **(G)** Adding a resistor between the harvesting pad and NPN transistor base (NPN-R) ex vivo in chicken breast increases the required applied voltage for switching (black = avg, grey = ind; n = 10). **(H)** Adding a capacitor between the base and emitter of an NPN transistor (NPN-C) ex vivo in chicken breast increases the required applied pulse length for switching (Avg ± SD; n=6-11). **(I)** Low voltage long pulses only trigger NPN + capacitor switches ex vivo in chicken breast while high voltage short pulses only trigger NPN + resistor switches. (R=2.2 kΩ; C= 1 μF; ind points, Avg ± SD, n=8). **(J)** Heat map of generated voltage potentials upon application of [6 V, 1 Hz, 200 μs] pulses across two hypodermic needles (gray circles) in ex vivo chicken breast models. **(K)** Voltage measured across each transistor's gate when moving the receiving pads away from the

signal injection source. Measurements taken at different pulse amplitudes. (line = Avg ± SD, n = 9). Scale Bars: B, C, K = 1 cm; D = 1 mm.

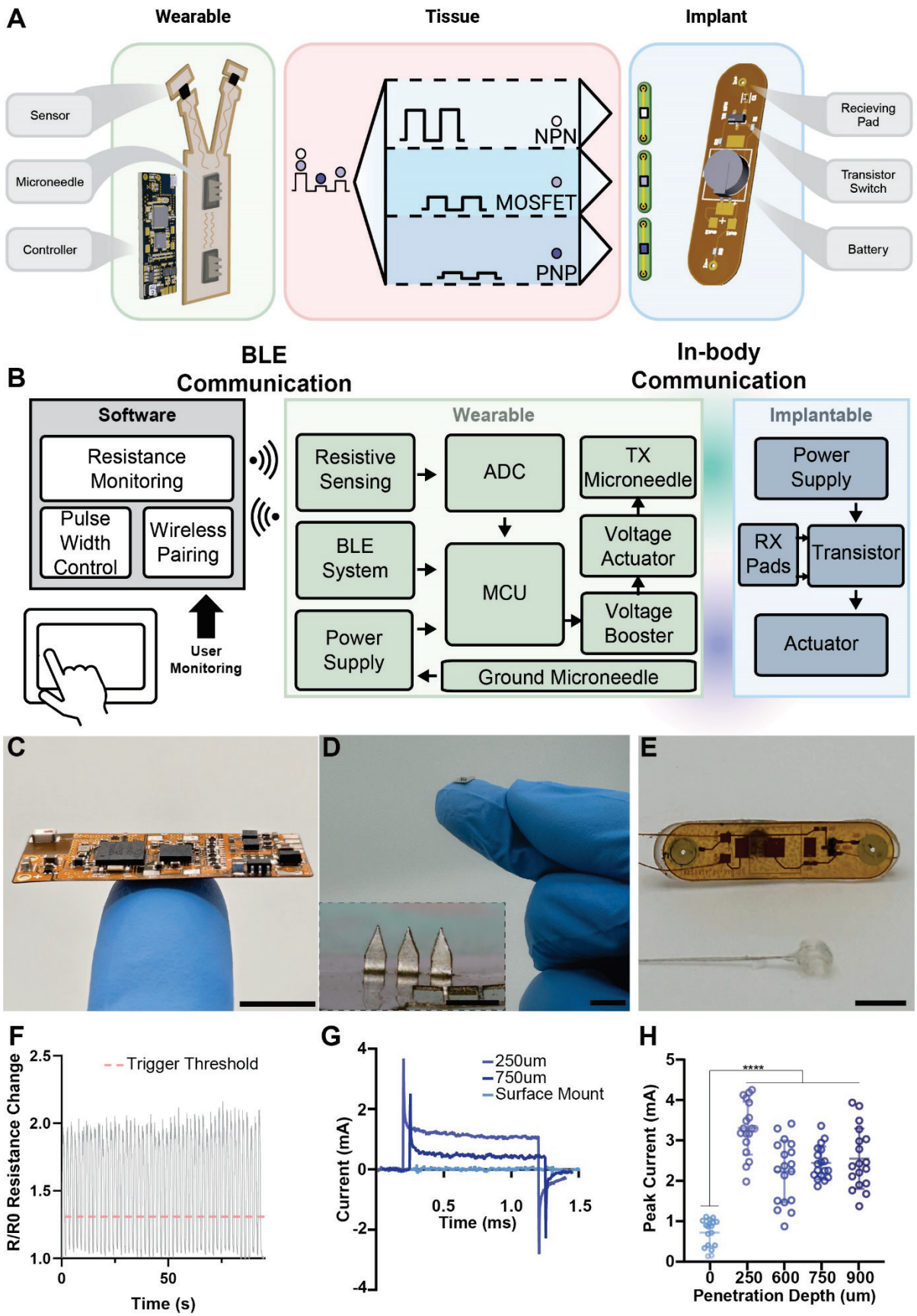
A
Wearable
Tissue
Implant
Sensor
Microneedle
Controller
NPN
MOSFET
PNP
Recieving Pad
Transistor Switch
Battery
B
BLE Communication
In-body Communication
Software
Resistance Monitoring
Pulse Width Control
Wireless Pairing
User Monitoring
Wearable
Resistive Sensing
ADC
TX Microneedle
BLE System
MCU
Voltage Actuator
Power Supply
Voltage Booster
Ground Microneedle
Implantable
Power Supply
RX Pads
Transistor
Actuator
C
D
E
F
Trigger Threshold
R/R0 Resistance Change
Time (s)
G
250um
750um
Surface Mount
Current (mA)
Time (ms)
H
****
Peak Current (mA)
Penetration Depth (um)

Fig. 2. In-body communication architecture. (A) A custom flexible printed circuit board (fPCB) continuously monitors a strain sensor and automatically emits a variable (0-12V) square wave pulse to trigger the implantable network. Bioelectronics can be switched individually or synergistically. **(B)** Block diagram for closed-loop control and monitoring of an implantable actuator via in-body ionic communication. **(C)** Photo of wearable fPCB. **(D)** Photo of stainless-steel microneedles that enable the wearable hub's signals to bypass the stratum corneum (inset scale bar = 1mm). **(E)** Photo of implantable fPCB with voltage receiving pads and a nerve cuff. **(F)** Cyclic testing of a laser-induced graphene (LIG) strain sensor with the threshold for wearable pulsing specified. **(G)** Representative [4 V, 1 Hz, 1 ms] square wave pulses in vivo in rats using skin-interfaced microneedle electrodes. **(H)** Peak injection current across microneedles in vivo in rats (n = 18 across 3 rats, SD plotted). Scale Bars = 1 cm.

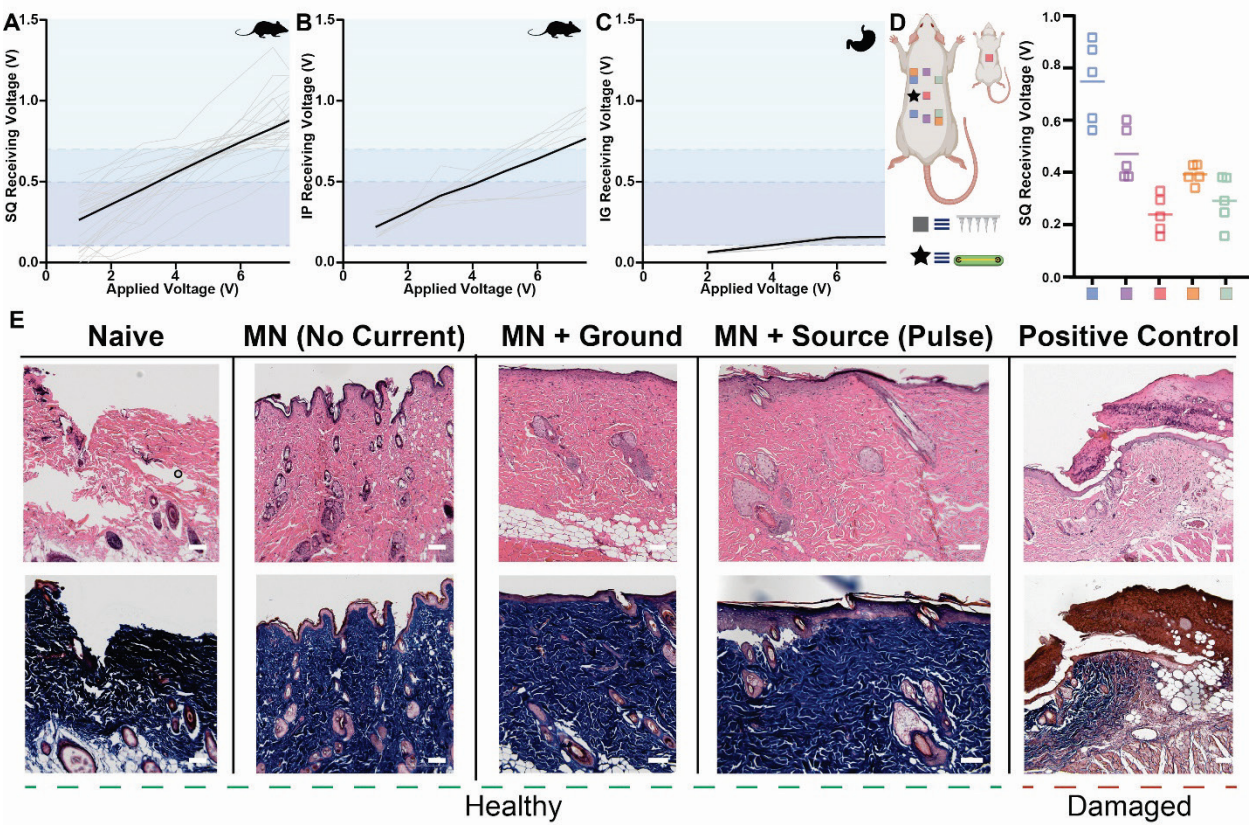

Fig. 3. In vivo in body communication generates intrabody voltage gradients without inducing cell trauma. (A-C) Voltage measured across a transistor's gate when applying increasing amplitude pulses across in vivo rat tissue. Receiving pads were placed 2.5 cm apart underneath the skin **(A)** or underneath the peritoneum **(B)** and V_{in} and Ground probes were placed 4 cm apart above the skin. In **(C)**, receiving pads were placed 1 cm apart inside the stomach. Shaded regions denote transistor gate and threshold voltages [black line = avg, grey line = individual tests; (A) n = 27 across 3 rats, (B) n = 9 across 3 rats, (C) n = 10 across 1 rat]. **(D)** Peak received voltage across receiving pads in vivo (n = 5 across 1 rat) when placed at varying orientations to the wearable signal injection probes. Receiving pads were placed 2.5cm apart underneath the skin. V_{in} and Ground probes were placed in spatially varied locations above the skin including in line with

the implant (blue), offset from the implant (purple), on the back and belly of the animal (pink), diagonally across the body (orange), and on the opposite side of the implant (green). **(E)** Representative H&E (top) and Masson's Trichrome (bottom) stained skin samples upon variable electromechanical treatments performed every other day for one week. Scar tissue formation (brown) is noted when applying 10 V and 100 ms pulses for two straight hours as a positive control, while other histology appears healthy, including when delivering pulses ≤ 10 V, ≤ 10 ms pulses, ≥100 times. Scale Bars = 0.1 mm.

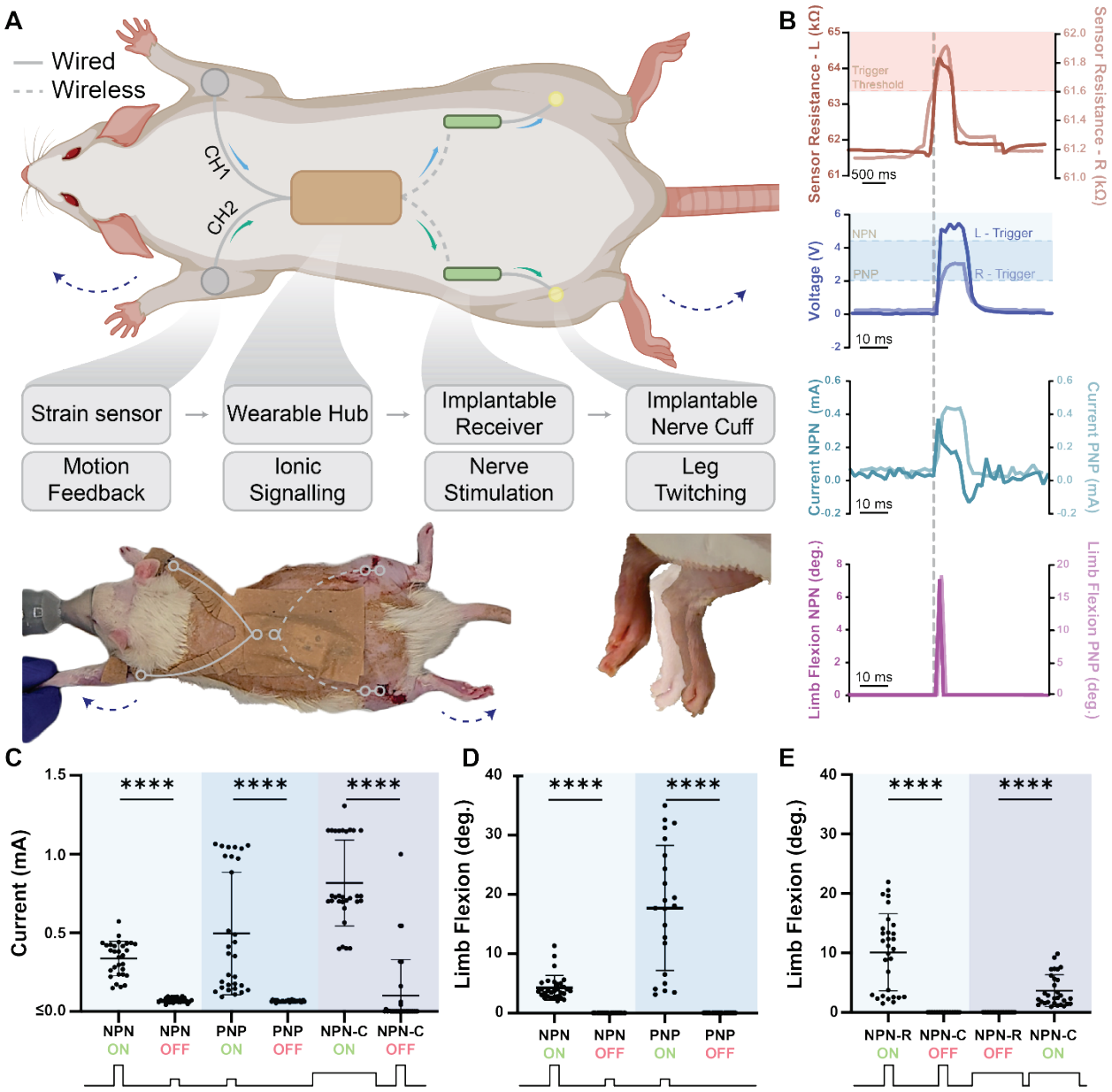

Fig. 4. Bio-integrated electronic networks for neurostimulation. **(A)** Schematic and image of rat outfitted with SWANS neurostimulator system with representative image of leg twitch from resting [translucent] to flexed [opaque]. **(B)** Upon stimulus detection on either forelimb, the wearable board outputs different pulse magnitudes and widths, which trigger different implants to actuate. **(C)** Current outputs from NPN implants using high V short pulses, from PNP implants using low V short pulses, and from NPN + Capacitor (NPN-C) implants using longer medium V

pulses. **(D)** Triggering the NPN and PNP implant combination led to sequential triggering of PNP only followed by NPN + PNP with increasing voltage when placed in the same animal. **(E)** NPN + Resistor (NPN-R) implants only triggered with High V short pulses and NPN-C implants only triggered with medium V long pulses when placed in the same animal. Pulse lengths and magnitudes varied across animals due to variance in skin thickness and tissue impedance, as described in Materials and Methods. (n=30 over 3 rats with different rats in each panel, Avg and SD plotted, **** indicates $p<0.0001$ in unpaired t-test with Welch's correction)

Acknowledgements: We are grateful to all members of the Abramson Lab for their helpful discussions. We thank Nathaniel Kirkpatrick, Richard Noel, and Laura O'Farrell for their help with animal experiment design. We are thankful to Alana Mermin-Bunnell for early discussions on the project. We thank the Parker H. Petit Institute for Bioengineering and Bioscience, School of Chemistry and Biochemistry, and the Office of the Executive Vice President for Research for their generous support. This work was performed in part at the Georgia Tech Institute for Matter and Systems, a member of the National Nanotechnology Coordinated Infrastructure (NNCI), which is supported by the National Science Foundation (Grant ECCS-2025462).

Funding: This work was funded in part by: the Georgia Tech Institute for Electronics and Nanotechnology 1000x seed grant (A.A., W.-H.Y.); an NSF GRFP fellowship (R.G.); the Georgia Tech President's Undergraduate Research Award (A.K.); the Georgia Tech Petit Scholars Research Award (E.F., A.C.); the Beckman Coulter Scholarship (A.C.); an NIH MIRA grant R35GM150689 (A.A.); the WISH Center grant from the Institute for Matter and Systems at Georgia Tech (W.-H.Y.); an NSF NRT-FW-HTF grant #2345860 (J.D., W.-H.Y.). A grant from the Research Foundation of Korea helped fund the time used for background research on the project (A.A.).

Author Contributions: R.G. and A.A. created the idea and designed the experiments supporting the development of SWANS. R.G. and E.F. performed the ex vivo characterization studies on ionic tissue communication in chicken breast tissue. R.G., E.K., Y.J.L., and G.B. designed and fabricated the printed circuit boards. R.G., E.F., and J.J. performed the in vivo experiments characterizing ionic tissue communication in rats. R.G., Y.J.L., G.B., and A.A. performed the in vivo neuromodulation experiments. A.A. and W.-H.Y. provided funding and supervised the project. All authors contributed to writing and editing the manuscript.

Competing Interests: A.A., R.G., Y.J.L., and W.-H.Y. are inventors on provisional patents describing the technology presented in this manuscript. A.A.'s full list of competing interests can be found at site.google.com/view/alex-abramson-coi.

Data Availability: All data associated with this study are present in the paper or the Supplementary Materials.

References

1. Mahato, K., et al., *Hybrid multimodal wearable sensors for comprehensive health monitoring*. Nature Electronics, 2024. **7**(9): p. 735-750.
2. Brasier, N., et al., *Applied body-fluid analysis by wearable devices*. Nature, 2024. **636**(8041): p. 57-68.
3. Nair, V., et al., *Miniature battery-free bioelectronics*. Science, 2023. **382**(6671): p. eabn4732.
4. Li, C., et al., *Design of biodegradable, implantable devices towards clinical translation*. Nature Reviews Materials, 2020. **5**(1): p. 61-81.
5. Nan, K., et al., *Mucosa-interfacing electronics*. Nature Reviews Materials, 2022. **7**(11): p. 908-925.
6. Park, J., et al., *Electromechanical convective drug delivery devices for overcoming diffusion barriers*. Journal of Controlled Release, 2024. **366**: p. 650-667.
7. Steiger, C., et al., *Ingestible electronics for diagnostics and therapy*. Nature Reviews Materials, 2019. **4**(2): p. 83-98.
8. Abdigazy, A., et al., *End-to-end design of ingestible electronics*. Nature Electronics, 2024. **7**(2): p. 102-118.
9. Bergenstal, R.M., et al., *A comparison of two hybrid closed-loop systems in adolescents and young adults with type 1 diabetes (FLAIR): a multicentre, randomised, crossover trial*. The Lancet, 2021. **397**(10270): p. 208-219.
10. Wadwa, R.P., et al., *Trial of Hybrid Closed-Loop Control in Young Children with Type 1 Diabetes*. New England Journal of Medicine, 2023. **388**(11): p. 991-1001.
11. Abramson, A., et al., *A flexible electronic strain sensor for the real-time monitoring of tumor regression*. Science Advances, 2022. **8**(37): p. eabn6550.
12. Du, W., et al., *Conformable ultrasound breast patch for deep tissue scanning and imaging*. Science Advances. **9**(30): p. eadh5325.
13. Choi, Y.S., et al., *A transient, closed-loop network of wireless, body-integrated devices for autonomous electrotherapy*. Science, 2022. **376**(6596): p. 1006-1012.
14. Al-Khatib, S.M., *Cardiac Implantable Electronic Devices*. New England Journal of Medicine, 2024. **390**(5): p. 442-454.
15. Ghanim, R., et al., *Communication protocols integrating wearables, ingestibles, and implantables for closed-loop therapies*. Device, 2023. **1**(3): p. 100092.
16. Farra, R., et al., *First-in-Human Testing of a Wirelessly Controlled Drug Delivery Microchip*. Science Translational Medicine, 2012. **4**(122): p. 122ra21-122ra21.
17. Ciatti, J.L., et al., *An autonomous implantable device for the prevention of death from opioid overdose*. Sci Adv, 2024. **10**(43): p. eadr3567.
18. Zhong, Y., et al., *Automated projection mode switching for glucose levels*. 2022, Google Patents.
19. Chung, H.U., et al., *Binodal, wireless epidermal electronic systems with in-sensor analytics for neonatal intensive care*. Science, 2019. **363**(6430): p. eaau0780.
20. Gilron, R.e., et al., *Long-term wireless streaming of neural recordings for circuit discovery and adaptive stimulation in individuals with Parkinson's disease*. Nature Biotechnology, 2021. **39**(9): p. 1078-1085.

21. Otsuka Pharmaceutical Development & Commercialization, I., *Protocol Title: An Open-label, Prospective Trial Assessing Positive Detection Accuracy and Detection Latency Measures of the Miniature Ingestible Event Marker Tablet Using the D-Tect Patch in Healthy Subjects and Assessing Detection Latency Measures Using the D-Tect Patch in Subjects With Serious Mental Illness Taking Abilify MyCite Tablet*. 2023.
22. Hafezi, H., et al., *In-body power source having high surface area electrode*. 2015, Google Patents.
23. Hafezi, H., et al., *An ingestible sensor for measuring medication adherence*. IEEE Transactions on Biomedical Engineering, 2014. **62**(1): p. 99-109.
24. Zhao, Z., et al., *Ionic communication for implantable bioelectronics*. Science Advances, 2022. **8**(14): p. eabm7851.
25. Maity, S., D. Das, and S. Sen, *Wearable health monitoring using capacitive voltage-mode Human Body Communication*. Annu Int Conf IEEE Eng Med Biol Soc, 2017. **2017**: p. 1-4.
26. Abramson, A., et al., *Ingestible transiently anchoring electronics for microstimulation and conductive signaling*. Science advances, 2020. **6**(35): p. eaaz0127.
27. Niu, S., et al., *A wireless body area sensor network based on stretchable passive tags*. Nature Electronics, 2019. **2**(8): p. 361-368.
28. Tian, X., et al., *Wireless body sensor networks based on metamaterial textiles*. Nature Electronics, 2019. **2**(6): p. 243-251.
29. Madhvapathy, S.R., et al., *Miniaturized implantable temperature sensors for the long-term monitoring of chronic intestinal inflammation*. Nature Biomedical Engineering, 2024. **8**(8): p. 1040-1052.
30. Sim, K.H., et al., *The appropriateness of the length of insulin needles based on determination of skin and subcutaneous fat thickness in the abdomen and upper arm in patients with type 2 diabetes*. Diabetes Metab J, 2014. **38**(2): p. 120-33.
31. Gill, H.S., et al., *Effect of microneedle design on pain in human volunteers*. The Clinical journal of pain, 2008. **24**(7): p. 585-94.
32. Cogan, S.F., et al., *Tissue damage thresholds during therapeutic electrical stimulation*. Journal of Neural Engineering, 2016. **13**(2).
33. Scheiner, A., J.T. Mortimer, and U. Roessmann, *Imbalanced biphasic electrical stimulation: muscle tissue damage*. Ann Biomed Eng, 1990. **18**(4): p. 407-25.
34. Fish, R.M. and L.A. Geddes, *Conduction of electrical current to and through the human body: a review*. Eplasty, 2009. **9**: p. e44.
35. Taylor, P.J., et al., *Tolerability and acceptability of real-time continuous glucose monitoring and its impact on diabetes management behaviours in individuals with Type 2 Diabetes - A pilot study*. Diabetes Res Clin Pract, 2019. **155**: p. 107814.
36. Won, S.M., et al., *Wireless and battery-free technologies for neuroengineering*. Nat Biomed Eng, 2023. **7**(4): p. 405-423.
37. Kim, J., et al., *Epidermal electronics with advanced capabilities in near-field communication*. Small, 2015. **11**(8): p. 906-12.
38. Awad, L.N., et al., *A soft robotic exosuit improves walking in patients after stroke*. Sci Transl Med, 2017. **9**(400).

39. Song, H., et al., *Continuous neural control of a bionic limb restores biomimetic gait after amputation*. Nat Med, 2024. **30**(7): p. 2010-2019.
40. Nadeau, P., et al., *Prolonged energy harvesting for ingestible devices*. Nature Biomedical Engineering, 2017. **1**(3): p. 0022-0022.
41. Abramson, A., et al., *An ingestible self-orienting system for oral delivery of macromolecules*. Science, 2019. **363**(6427): p. 611-615.
42. Huang, H.-W., et al., *An implantable system for opioid safety.* Device, 2024. **2**(10).
43. Mickle, A.D., et al., *A wireless closed-loop system for optogenetic peripheral neuromodulation*. Nature, 2019. **565**(7739): p. 361-365.
44. Bansal, A., S. Shikha, and Y. Zhang, *Towards translational optogenetics*. Nat Biomed Eng, 2023. **7**(4): p. 349-369.
45. Krishnan, S.R., et al., *A wireless, battery-free device enables oxygen generation and immune protection of therapeutic xenotransplants in vivo.* Proc Natl Acad Sci U S A, 2023. **120**(40): p. e2311707120.
46. Lee, I., et al., *Electrocatalytic on-site oxygenation for transplanted cell-based-therapies*. Nat Commun, 2023. **14**(1): p. 7019.
47. Rivnay, J., P.E. Sheehan, and O. Veiseh, *Are implantable, living pharmacies within reach?* Science, 2024. **386**(6719): p. 271-273.
48. Li, G., S. Wang, and Y.Y. Duan, *Towards conductive-gel-free electrodes: Understanding the wet electrode, semi-dry electrode and dry electrode-skin interface impedance using electrochemical impedance spectroscopy fitting*. Sensors and Actuators B: Chemical, 2018. **277**: p. 250-260.

Supplementary Materials for

An artificial nervous system for communication between wearable and implantable therapeutics

The following includes:

Materials and Methods

Figs. SI1 to SI7

Supplementary Information

Materials and Methods

Transistor switching experiments with ex vivo chicken breast

Chicken breast (150-200g, Heritage Farms) was soaked in PBS (VWR) for up to two hours. Using a function generator (Siglent - SDG2000X), 1 Hz monophasic pulses of various amplitudes were applied across 13 cm of tissue. Voltage generation and harvesting were accomplished with hypodermic needles (BD) or laser-cut stainless-steel shim (McMaster-Carr) as described in "Fabrication of Microneedles" below. Receiver pads were positioned on the tissue surface at various separations between the signal injecting and grounding probes including pad separations of 9, 5, 3, and 0.5cm.

Applied and harvested voltages, along with current through a 100Ω shunting resistor, were measured using an oscilloscope (Rigol-MSO5000). Current was measured by probing both sides of the resistor, smoothing the data to remove noise by taking a 10-point moving average, and measuring the peak difference between the voltage measurements during the pulse. The max current was reported ex vivo; for in vivo experiments, the max average current over a 50 µs period, the time required to enable a leg twitch, was recorded. 3 transistors including a 2N2222 (NPN), 2N2907 (PNP), and a P55NF06L (MOSFET) were connected in series with a 3V battery and an LED to determine required applied voltages to reach the active and saturation regions of each transistor. To construct a visual representation of the generated voltage gradients, potentials were collected at various locations across the tissue with respect to a grounding tissue-interfaced electrode.

Surface area experiments with ex vivo chicken breast

Chicken breast was soaked in PBS (VWR) for up to two hours. Using a function generator, 1 Hz monophasic pulses of various amplitudes were applied across 13 cm of tissue. 10 mm^2 stainless steel electrodes were directly connected to the function generator. Various sized electrodes (1, 2, 3, 5, 7.5, and 10 mm^2) were placed 9cm apart to capture a portion of the generated gradient. Harvested potentials were recorded with an oscilloscope.

Device Fabrication

Fabrication and characterization of the Wearable package: A wearable pulse generation system was developed, featuring a flexible PCB (fPCB) circuit layered with polyimide-copper for skin conformity and flexibility. The wearable device connects with an Android application, allowing contactless control of pulse delivery and custom adjustments of parameters such as frequency (0.01-1 Hz) and pulse width (1-1000 ms). The fPCB utilizes the nRF52832 microcontroller (MCU) architecture, selected for its industry standard low-power Bluetooth capabilities. This wireless system integration allows user-defined control via the mobile app for open/close/remote controls.

The device's voltage range spans from 1V to 12V, powered by a custom-configured, controllable DC-DC step-up voltage regulator and booster. A DC-DC boost converter that steps up the LiPo battery voltage (3.7V nominal) to the custom stimulation voltage (0-12V adjustable). The design is customizable with stimulation scenarios using both transistors and MOSFETs, regardless of NPN or PNP types, allowing for programmable voltage amplitude, pulse width, and frequency to generate dynamic pulses. A set of power switch drivers generates user-programmable monophasic or biphasic pulses that can be controlled by firmware code, making the device fit for various stimulation protocols. The system-on-chip placed at the center of the PCB processes executing the main control algorithm, reading sensor data, and driving the stimulation pulses.

To facilitate input-triggered reading/actuation, an ADS1292 24-bit analog-to-digital converter (ADC) is integrated, interfacing with resistive sensing elements. These elements detect mechanical stimulation, such as strain changes, and can initiate pulse generation in response to physical cues and for biofeedback system. The system is designed with minimal traces length and physical hardware for data communication, operation, and critical signals. The ground planes are separated to reduce electromagnetic interference and/or logic interference and/or control interference. Flexible serpentine traces interface with the LIG sensor and are designed to maintain mechanical compliance and reduce stress at joints of the pads. The strain that was continuously measured by a Wheatstone-type resistor network of resistor branches with adjustable reference thereby allows differential resistance sensing and fine-tuning of offset and gain for further calibration, calibration curve, and measurement precision.

All firmware and software development were conducted in a Windows desktop environment. Firmware is compatible with Nordic nRF52 platform Soft Device stack for BLE functionality and acknowledgement. The companion mobile application was implemented in Kotlin (2022) for Android devices, tested performed on a Samsung Galaxy S8 tablet.

Fabrication and characterization of the Implantable package: The implantable device, measuring 25 by 10 mm, is designed to function as a subdermal signal receiver and programmable output stimulator. The device is powered by a 6.8 mm diameter 1.55V silver oxide coin cell battery (Duracell 377), a 4.8 mm diameter 3V lithium coin cell battery (Seiko Instruments, ML414H IV01E), or a 10 mm 3V lithium coin cell battery (Fuspower, CR1025) selected for their compatibility with gate voltage requirements and operational lifetime. The entire implantable fPCB is encapsulated in PDMS (Sylgard 184, Dow) using a 2-piece mold that ensures that gold contact pads for signal harvesting interface with surrounding tissue. Loctite 4311 medical grade epoxy coating could further isolate the electronics from the surrounding tissue. The stimulation is programmable through the GPIO of the wearable's microcontroller, allowing dynamic control over the applied stimulation parameters. For signal modulation, the implantable system supports selective use of NPN, PNP, or MOSFET components to regulate the gate voltage and control the current passing through the implantable. It also possesses location to add resistors between the harvesting pads and transistor gate, as well as capacitors between the base and emitter as needed.

Fabrication of Microneedles*:* 75μm stainless-steel shim (McMaster-Carr; 316SS) was laser-cut using a femtosecond laser-cutter (60W, 75% power, 150 repetitions, or 4W, 60 kHz, 100% power, 45 repetitions, Optec). Microneedles were manually prodded out using a razor blade or hypodermic needle. Microneedles were cleaned and electropolished using a 6:3:1 glycerin:85% phosphoric acid: DI water.

Laser-Induced Graphene sensor fabrication and characterization. The fabrication of the uniaxial LIG sensor began with the synthesis of styrene-ethylene-butylene-styrene (SEBS) in a dissolution concentration at 5%, homogenized on a hotplate at a determined temperature for a precise duration to ensure uniform solution characteristics. The stainless steel (SS) substrate was prepared by spraying it with an anti-stick aerosol (Ease Release 200, Reynolds Advanced Materials) to ease subsequent material removal. SEBS solution was then drop-cast onto the SS substrate and cured at 35°C for 2 hours, resulting in a uniform SEBS film. Laser micromachining using the OPTEC Femtosecond Laser was employed to achieve precise film patterning, after which the negative material was carefully removed. For the LIG component, a polyimide (PI) sheet of 75 um thickness underwent CO_2 laser cutting at 5% power (Trotec Speedy laser, 5% power, 0.2 speed, 16 kHz), which induced the formation of graphene layer on its surface. The LIG strip was transferred onto the stretchable SEBS substrate and PI/Cu interconnect layer through mechanical stamping, with pressure applied at 100N over ten repetitions to ensure strong adhesion. The interconnect and LIG components were then sealed together by SEBS-SEBS film adhesion, which relies on Van der Waals forces for a secure bond, achieving both durability and stretchability without increasing overall thickness. Finally, the exposed copper pads of the PI/Cu interconnect were soldered to the 2CH lead from the device, and the entire assembly was bonded to a fabric adhesive for secure mounting onto biological substrates.

To measure the resistance during stretching, we attached the samples to a homemade stretching station and connected the samples to a tabletop multimeter. A custom LabView program simultaneously collected force, displacement, and resistance data. Samples were stretched at 1mm/s up to 20% strain for up to 50 cycles.

To characterize on-body performance, a laser-induced graphene (LIG) sensor is affixed to the skin of the small animal using brown medical tape. The LIG strain sensor displays a gauge factor of 5-10 demonstrates large relative resistance changes with only small mechanical deformations (<5% strain). In practical terms, these sensors can detect subtle limb or finger movements down to sub-millimeter displacements. The minimum resolvable strain can be as low as 0.5% in the presence of environmental noise.

Fabrication of Bi-layer Copper Flexible 2CH Interconnect: Sylgard 184 (Dow) with a 10:1 PDMS to crosslinker ratio was prepared. The prepared PDMS was subsequently spin-coated onto a stainless-steel substrate to ensure a smooth surface, set at a speed of 1000 rpm for a duration of 35 seconds, with a ramp period of 5 seconds included. The elastomer was then cured at 120°C on a hotplate for 30 minutes. A copper (Cu) foil was laminated onto the PDMS surface; due to the

inherent Van der Waals forces, no additional adhesive was required to achieve adhesion, attributed to the high adhesion energy of PDMS molecules that promote stable interfacial contact.

Following the initial lamination, a layer of low-modulus silicone elastomer with high surface energy (Ecoflex-GEL, Smooth-On Inc.) was applied on the laminated Cu film via spin coating at 1500 rpm for 35 seconds. The applied elastomer was then cured at 65°C for 1 hour, providing a uniform insulating layer. Subsequently, a second Cu foil was laminated onto the cured elastomer layer, resulting in a bi-layer configuration of parallel Cu films separated by a thin elastomer layer that serves as an insulator to prevent electrical shorting.

To pattern the Cu-elastomer-Cu composite, laser micromachining was performed using an OPTEC Femtosecond Laser system. A multi-step cutting process was employed to minimize substrate damage when processing the relatively thick composite layer. Using the top Cu film as the baseline focal point, patterning was conducted at 65% laser power for five repetitions. The focal point was then lowered by 250 μm, and the cutting process was repeated. This sequence was iterated three times to ensure full penetration through the composite to the bottom Cu layer. After laser processing, negative material was carefully removed, and the resulting bi-layer interconnect was laminated with PVA water-soluble tape (5414 Water-Soluble Wave Solder Tape, 3M) to facilitate its transfer from the PDMS surface for further integration onto fabric adhesive substrates.

Fabrication of PI/Cu Flexible Interconnect: The PDMS precursor was prepared with Sylgard 184 (Dow) at a 10:1 PDMS to crosslinker ratio and then spin-coated onto a stainless-steel substrate at 1000 rpm for 35 seconds, including a 5-second ramp, to achieve a smooth elastomer layer. Curing was conducted on a hotplate at 120°C for 30 minutes. After curing, Cu foil was laminated onto the PDMS surface, where it adhered naturally due to Van der Waals forces, facilitated by the high adhesion energy of PDMS molecules.

Following Cu lamination, a heat-activated polyimide (PI) adhesive film (Pyralux LF, DuPont) was applied onto the Cu foil, and bonding between the Cu and PI layer was achieved by heat pressing at 400°C for 15 seconds. The thermoplastic adhesive was activated under heat, forming a cross-linked polymer matrix between the PI and Cu layers, thereby creating a permanent bond.

The PI/Cu composite film was subsequently patterned using laser micromachining with an OPTEC Femtosecond Laser at 75% power, applied in five repetitions. The laser cutting parameters were meticulously optimized to remove material effectively while preventing thermal damage, which could introduce carbonized impurities along the patterned edges. Upon completion of the laser patterning, the negative material was removed, and the remaining bi-layer interconnect was laminated with PVA water-soluble tape (5414 Water-Soluble Wave Solder Tape, 3M) to facilitate detachment from the PDMS substrate and subsequent transfer to a fabric adhesive for final mounting.

<u>Voltage Receiving Simulation</u>

$\nabla \cdot D = \rho_v$ (1)
$E = -\nabla V$ (2)

Geometry generation and E-field distribution analysis simulations were performed using the commercial finite element method (FEM) software, COMSOL Multiphysics version 6.2. (Burlington, MA, USA) To simplify the modeling procedure, a pair of microneedle pads, an implant-receiving pad, and the skin were implemented in the simulation. The relative permittivity of the skin was 6000, and the electrical conductivity was set as 0.1 S/m. The microneedle pads were selected as iron, which had a relative permittivity of 4 and the electric conductivity of 10.2×10^6S/m referenced from the COMSOL material library. The receiving pad from the implantable device was set to gold, which has a relative permittivity of 5, and electrical conductivity was set as 45.6×10^6S/m, also referenced from the COMSOL material library. The electrostatic equation was used for the electric potential simulation. It is defined by Eq. (1) and Eq. (2).

OECT Fabrication

OECT devices with dimensions of L = 5 μm and W = 400 μm were fabricated in the cleanroom environment. Source and drain electrodes were defined using photolithography with AZnLOF2020 photoresist and a mask-less aligner (Heidelberg MLA 150). A 10 nm layer of Ti followed by a 100 nm layer of Au was deposited by using an e-beam evaporator (Temescal FC2000). Subsequently, a first layer of parylene-C was deposited using a Specialty Coating Systems PDS 2010, employing Silane A174 (Sigma-Aldrich) as an adhesion promoter. A sacrificial layer of 2% MICRO-90 soap (VWR) in DI water was spin-coated onto the wafer before depositing a second layer of parylene-C. The channel and electrode pads were then defined using the same maskless aligner with AZ10XT photoresist and a reactive ion etching process (SAMCO 230iP). Channels were formed by spin-coating a 5 mg/mL solution of a semiconducting polymer, poly[(2,6-bis(thiophen-2-yl)-3,7-bis(9-octylnonadecyl)thieno[3,2-b]thieno[2',3':4,5] thieno[2,3-d]thiophene-5,5'-diyl)-alt-(3,6-bis(thiophen-2-yl)-2,5-bis(8-octyloctadecyl)pyrrolo[3,4-c]pyrrole-1,4(2H,5H)-dione)-5,5'-diyl] or DPP-4T (Corning Incorporated), onto the devices at 2000 rpm for 35 s via dynamic spin-coating. Following a peel-off step, the devices were baked inside a glovebox at 120 °C for 30 min and allowed to cool for at least 1 h before characterization. A PDMS sheet was cut to form a well and used to contain the 1-ethyl-3-methylimidazolium bis(trifluoromethylsulfonyl)imide (Sigma-Aldrich) electrolyte. Transfer characteristics, as well as responses to a pulse burst, of the OECT devices were then measured with an Ag/AgCl pellet as the gate using a Keithley 4200A. Data were plotted using OriginLab software.

In vivo signal injection characterization

All animal procedures were approved by the Georgia Institute of Technology Institutional Animal Care and Use Committee and conducted in accordance with Georgia Institute of Technology animal facility guidelines. Adult male and female Sprague Dawley rats (200-300g; Charles River Laboratories, Wilmington, USA) were maintained on a 12h:12h light:dark cycle (lights on at 7:00).

Subjects were anesthetized and placed in a lateral recumbent position. 2 patches of skin separated by 4cm were shaven and cleaned aseptically. Various electrodes (surface mounted – 0µm penetration, 300µm, 600µm, 750µm, 900µm, and 1600 µm) were connected to a function generator in series with a 100Ω resistor. 1 Hz, monophasic, 4V pulses were used to generate voltage gradients across the rat and the injected current was measured.

Additionally, the injected current using 900µm microneedles was quantified for a range of applied voltages from 0.5V – 10V.

Transistor switching experiments in vivo: Subjects were shaven and prepared for aseptic surgery using 3 cycles of chlorohexidine and 70% ethanol application. A 1cm incision was made perpendicular to the animal torso halfway between the animal's fore- and hindlegs. 1mm diameter gold coated PDMS pads (300rpm, 10:1 ratio cured at 70°C; SYLGARD 184, Dow, Midland, USA) were placed inside the subcutaneous space on either side of the incision at a separation of 2.5 cm. The incision was closed temporarily with sutures (4-0 silk, Covidien) to prevent the subcutaneous space from drying. Microneedles were applied onto the skin 0.75 cm away from each of the implanted conductive pads and connected directly to a function generator. Applied and harvested voltages were measured as described previously.

Additionally, transistor switching was performed by placing these gold pads on the peritoneal lining simulating an implantable device placed in the intraperitoneal space. Finally, the gold pads were placed inside the stomach by exteriorizing the stomach, making a 0.5cm incision and placing the pads inside the stomach. Afterwards, the stomach was placed back inside the intraperitoneal space.

NPN-R and NPN-C transistors that demonstrated independent switching in vivo required different pulse lengths, resistances, capacitances, voltage magnitudes, microneedle lengths, and microneedle locations depending on the animal. In each animal, these values remained the same throughout the entire data collection experiment to ensure that the switching only occurred due to the changes between two defined pulses. In animal 1, a female rat with thinner skin, the settings were as follows: 422Ω Resistor; 68 pF Capacitor; 10 V / 250 µs pulse to turn on the NPN-R implant; 6.5 V / 2 ms pulse to turn on the NPN-C implant; 900 µm microneedle length. In animal 2, a male rat with thicker skin, the settings were as follows: 825Ω Resistor; 47 pF Capacitor; 10 V / 100 µs pulse to turn on the NPN-R implant; 8.0 V / 1.2 ms pulse to turn on the NPN-C implant; 1600 µm microneedle length. In animal 3, a male rat with thicker skin, the settings were as follows: 825Ω Resistor; 47 pF Capacitor; 4.1 V / 150 µs pulse to turn on the NPN-R implant; 3.2 V / 2 ms pulse to turn on the NPN-C implant; 1600 µm microneedle length.

Closed-loop demonstration via in-body communication: Subjects were shaven and prepared for aseptic surgery using 3 cycles of chlorohexidine and 70% ethanol application. Female Sprague Dawley rats (200-300g, Charles River) were anesthetized with 2% isoflurane in balanced oxygen. Under sterile conditions with external body warming, a 2-cm incision was made on the left and right thigh. About 1 cm of the sciatic nerve proximal to the tibial and peroneal bifurcation was

inserted into the nerve cuff electrode (NC-2-2-125SS-1.5-2-00-300-00, MicroProbes). Nerve cuff leads were tunneled through the muscle layer (closed with 4-0 silk sutures (Ethicon)) into the subcutaneous space where the implantable FPCB was placed. The skin was secured with sutures.

The subject was placed in a prone position and was outfitted with the wearable FPCB including microneedles and a soft strain sensor. A soft tether was applied to each of the forelimbs and the tether was controlled by the researcher to simulate extension of the forelimb and a natural walking motion. Electrical characterization of the wearable and implantable FPCBs was completed using an oscilloscope. Resistance measurements were collected using a tabletop multimeter (Keithley). Frames from video recordings set up for monitoring each of the hindlegs were extracted and used to determine the degree of limb flexion.

The wearable and implantable devices operate in a closed-loop configuration for adaptive therapeutic response. The wearable device continuously monitors motion through a Laser-Induced Graphene (LIG) sensor, capturing motion range and detecting boundary conditions. Upon detecting a boundary condition change, the wearable's pulse generator activates a voltage boost, sending an electrical trigger to the implantable device.

This closed-loop control enables targeted neurostimulation via a microneedle interface in the implantable system, precisely adjusting the stimulation intensity in response to user movement or external stimuli. The implantable device, acting as an electrical gate, modulates the stimulus through programmable parameters, ensuring effective and responsive therapy delivery within the in vivo model.

Tissue Health and Histological Examination Studies of applied voltage

For examination studies, microneedles were applied to rat skin in vivo and stimulated with 100 pulses by the wearable FPCB or a function generator and imaged with an optical microscope immediately after the pulses and again after 3 hours. For hematoxylin/eosin (H&E) staining and Masson's Trichrome staining, the tissue was either paraffin embedded or frozen. For paraffin embedded samples, tissue samples were fixed overnight in 10% formalin buffer, then dehydrated by an automatic tissue dehydration system. The dehydrated tissue was embedded in paraffin and sectioned at 5um thickness by rotary microtome. For frozen samples, rat skin tissue samples were immediately embedded in optimal cutting temperature compound (Sakura Finetek, CA), frozen with dry ice, and sectioned at 5 μm thickness with a cryostat. Stained slides were imaged using an inverted microscope.

SI 1. BLE current consumption profiling and power consumption comparison across communication methods. (A) Representative BLE current profile measured using the nRF Profiler, illustrating average and peak current consumption during discrete operational stages: pre-processing, ramp-up, standby, radio startup, RX (receiving), radio switching, TX transmission, and post-processing. (B) Comparative summary of theoretical and experimental power consumption metrics (mean ± SD, n = 3) for Implantable transistor-based system, Bluetooth Low Energy (BLE), and Near Field Communication (NFC) communication. The table highlights standby currents, active currents, daily power consumption, and estimated battery lifetimes for each technology, demonstrating the substantial energy-saving advantages of the implantable transistor-based system compared to BLE and NFC.

A

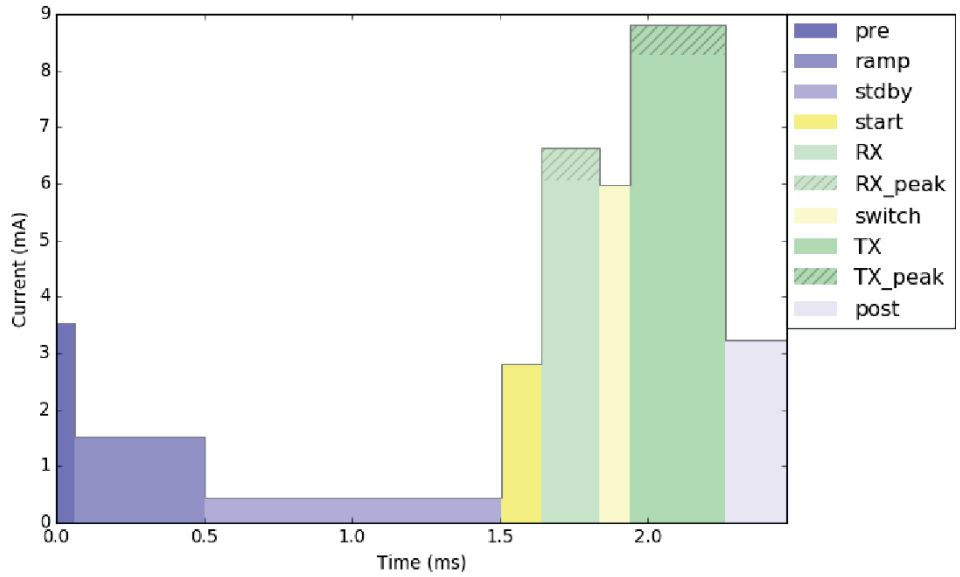

Stage	Description	Time (ms)	Length (us)	Avg. current (mA)	Peak current (mA)
pre	Pre-processing	0.0	61	3.5	
ramp	Standby + HFXO ramp	0.1	440	1.5	
stdby	Standby	0.5	1004	0.4	
start	Radio startup + CPU	1.5	133	2.8	
RX	Radio RX	1.6	200	6.0	6.6
switch	Radio switch	1.8	102	6.0	
TX	Radio TX	1.9	323	8.3	8.8
post	Post-processing	2.3	205	3.2	
	System On IDLE	2.5	1997.5 ms	2.0 uA	
Total			**2000.0 ms**	**5.4 uA**	

B

Scenario	Parameter	Theoretical Consumption	Experimental Consumption (Mean ± SD, n=3)	Estimated Battery Life (Mean ± SD)
In Body Communication (IBC)	Standby Current	1 μA × 1.55 V = 1.55 μW	1.2 ± 0.1 μW	281 ± 10 days
	Active Current	5 mA × 1.55 V = 7.75 mW	7.8 ± 0.5 mW	
	Daily Consumption	0.134 mWh	0.140 ± 0.02 mWh	
Bluetooth Low Energy (BLE)	Standby Current	2 μA × 3.0 V = 6 μW	6.5 ± 0.5 μW	40 ± 5 days
	Active Current (TX)	8.3 mA × 3.0 V = 24.9 mW	25 ± 1 mW	
	Daily Consumption	~1.5 mWh	1.5 ± 0.2 mWh	
Near Field Communication (NFC)	Standby Current	5 μA × 3.3 V = 16.5 μW	17 ± 1 μW	31 ± 2 days
	Active Current	20 mA × 3.3 V = 66 mW	65 ± 2 mW	
	Daily Consumption	2 mWh	2.1 ± 0.3 mWh	

SI 2. Organic electrochemical transistors (OECTs) enable digital switching and long-term drain current after pulsing. (A) OECT response to 10 pulses of 100ms pulses [0, -0.8 V, 50% duty cycle (ED)], V_{ds} -0.6 V. (B) OECT response to 10 pulses of 1s [0, -0.8 V, 50% ED], V_{ds} = -0.6 V (C) First 10 transfer curves of a DPP-4T-based OECT device in EMIM-TFSI. (D) OECT response to 1 pulse of 100ms pulse [0, -0.8 V, 0.5 Hz] applied to ex vivo chicken breast model, V_{ds} -0.6 V. (F) OECT used to switch on/off an LED using an ex vivo chicken breast model.

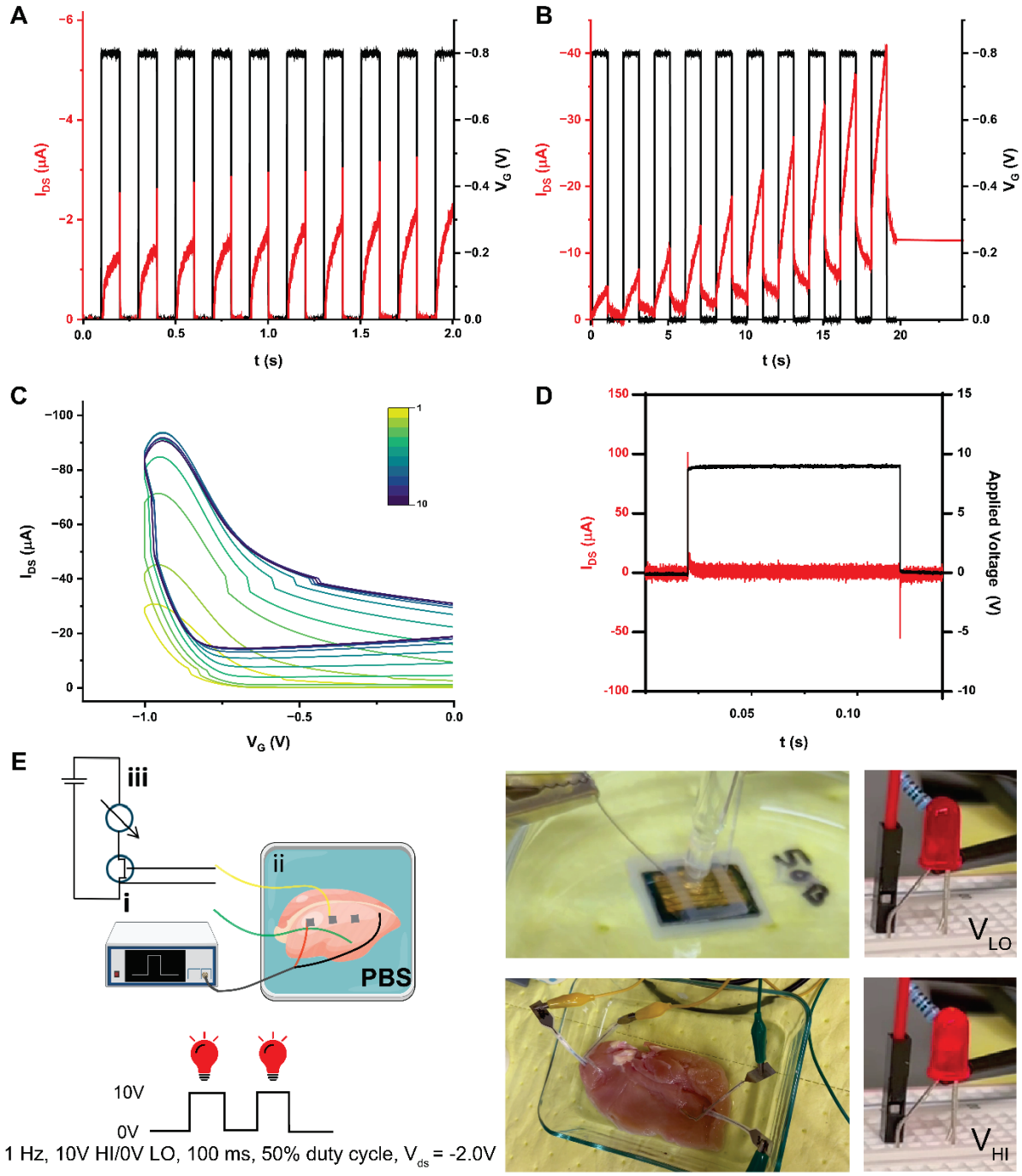

SI 3. Continued ex vivo characterization of in-body communication and transistor switching. (A) Receiving pads are maintained at a constant distance of 3cm, while the signal injection pad are varied from 1, 2, and 5cm from the receiving pad. (Black lines = mean, n=3). (B) Various receiving pad surface areas at a constant applied voltage of 7V and separation of 3cm between receiving pads.

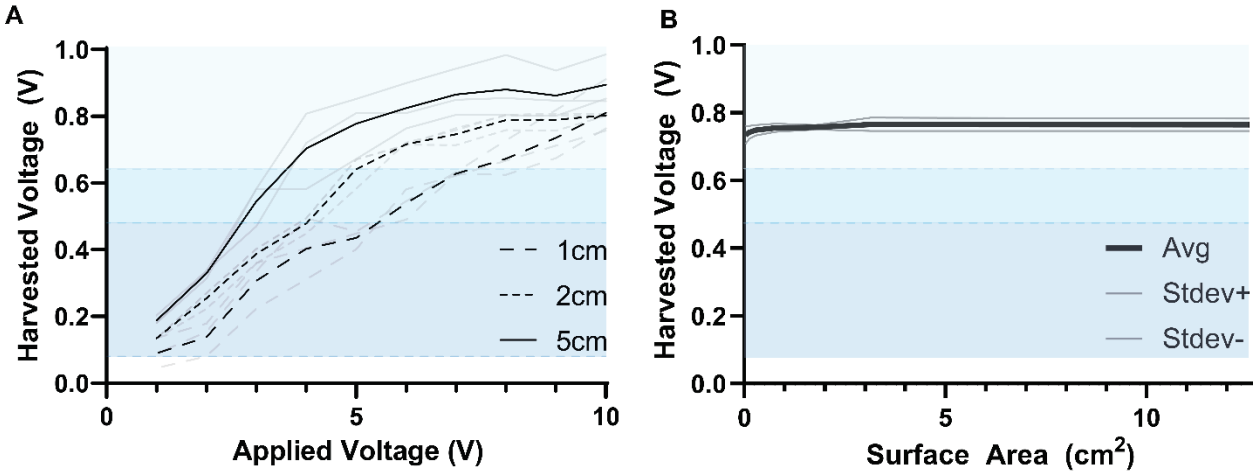

SI 4. **COMSOL simulations of electric-field generation in rat- and human-model tissue.** (A) Transmitter pads create an electric field and generate voltage gradients across centimeter-scale model tissue. Receiving pads detect these voltage gradients as a function of pad orientation, spatial position, and separation. (B) Electric field generation in rat-model tissue. (C) Electric field generation in human-model tissue. (Next page) Voltage gradients as a function of pad orientation, spatial position, and separation at applied voltages of 3 V and 7 V.

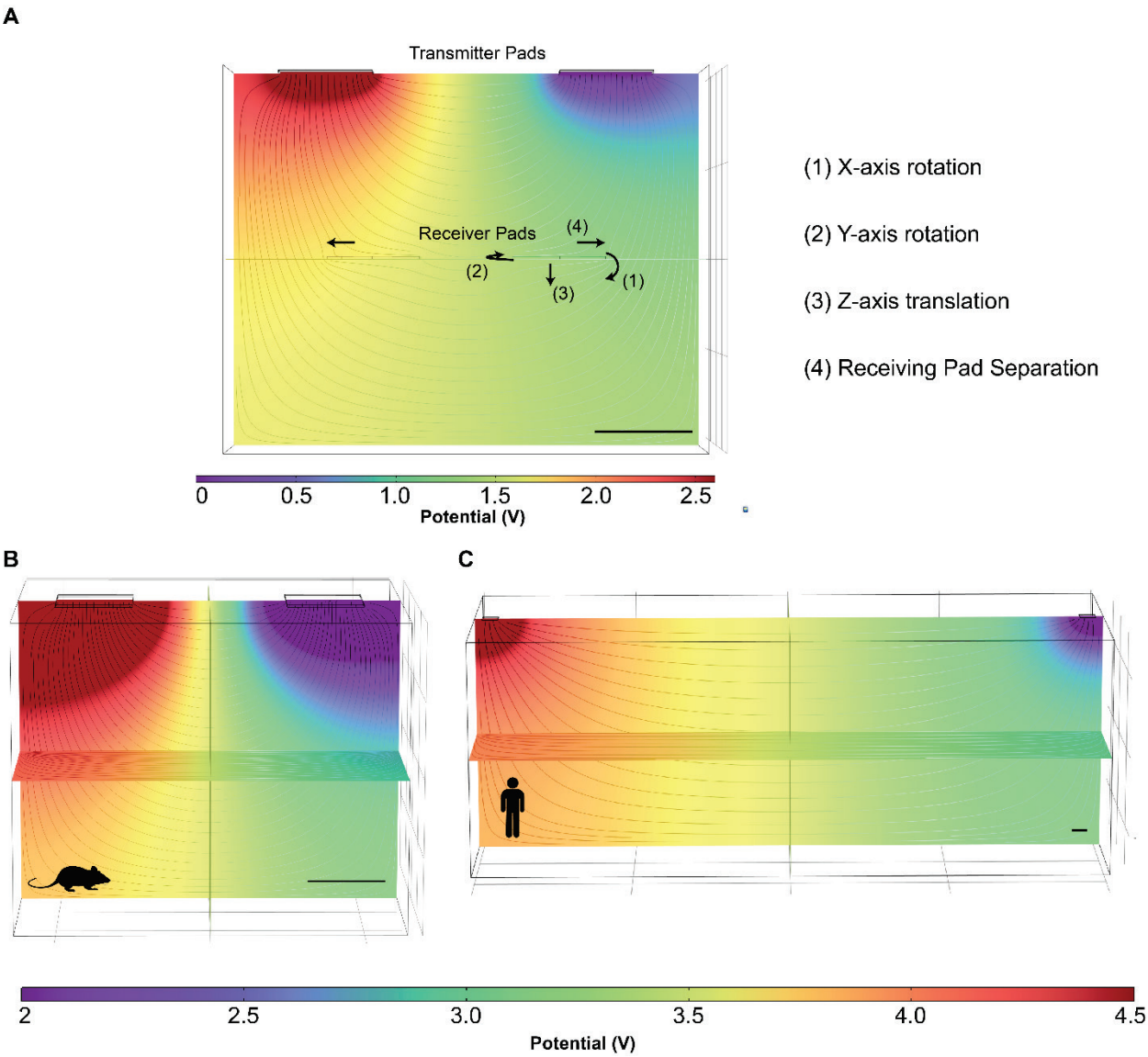

Receiving Pad Transformation	Applied Voltage (V)	Configuration	Receiving Voltage (dV, V)
(1) X-axis Rotation	**3**	**In-line (0°)**	**0.5**
		Offset (30°)	0.5
		Offset (60°)	0.49
	7	In-line (0°)	1.18
		Offset (30°)	1.17
		Offset (60°)	1.15
(2) Y-axis Rotation	**3**	**In-line (0°)**	**0.50**
		Offset (30°)	0.44
		Offset (60°)	0.26
	7	In-line (0°)	0.50
		Offset (30°)	1.02
		Offset (60°)	0.60
(3) Z-axis Translation	**3**	**2 cm**	**0.50**
		3 cm	0.30
		4 cm	0.24
	7	2 cm	1.18
		3 cm	0.69
		4 cm	0.56

Applied Voltage (V)	Receiving Pad Separation	Receiving Voltage (dV, V)
3	**2 cm**	0.50
	3 cm	0.58
	4 cm	0.68
7	2 cm	1.18
	3 cm	1.36
	4 cm	1.58

SI 5. Multiplexed wireless sensing wearable and implantable. (A) Wearable "hub" PCB illustrating key components: nRF52832 MCU (BLE communication), ADC converter (sensor data readout), resistive sensing pads, configurable voltage booster for high-voltage pulse actuation, and integrated BLE antenna. (B) PCB fabrication layout highlighting the wearable hub's electronic components and separated ground design. (C) Implantable PCB featuring coin-cell battery, transistor switch, actuator, and receiving pads for triggering via in-body signals. Optional locations for resistors between the transistor base and receiving pad and capacitor between the transistor base and emitter are marked. (D) Android application interface demonstrating real-time monitoring of resistive sensor data and manual pulse stimulation control, providing wireless communication.

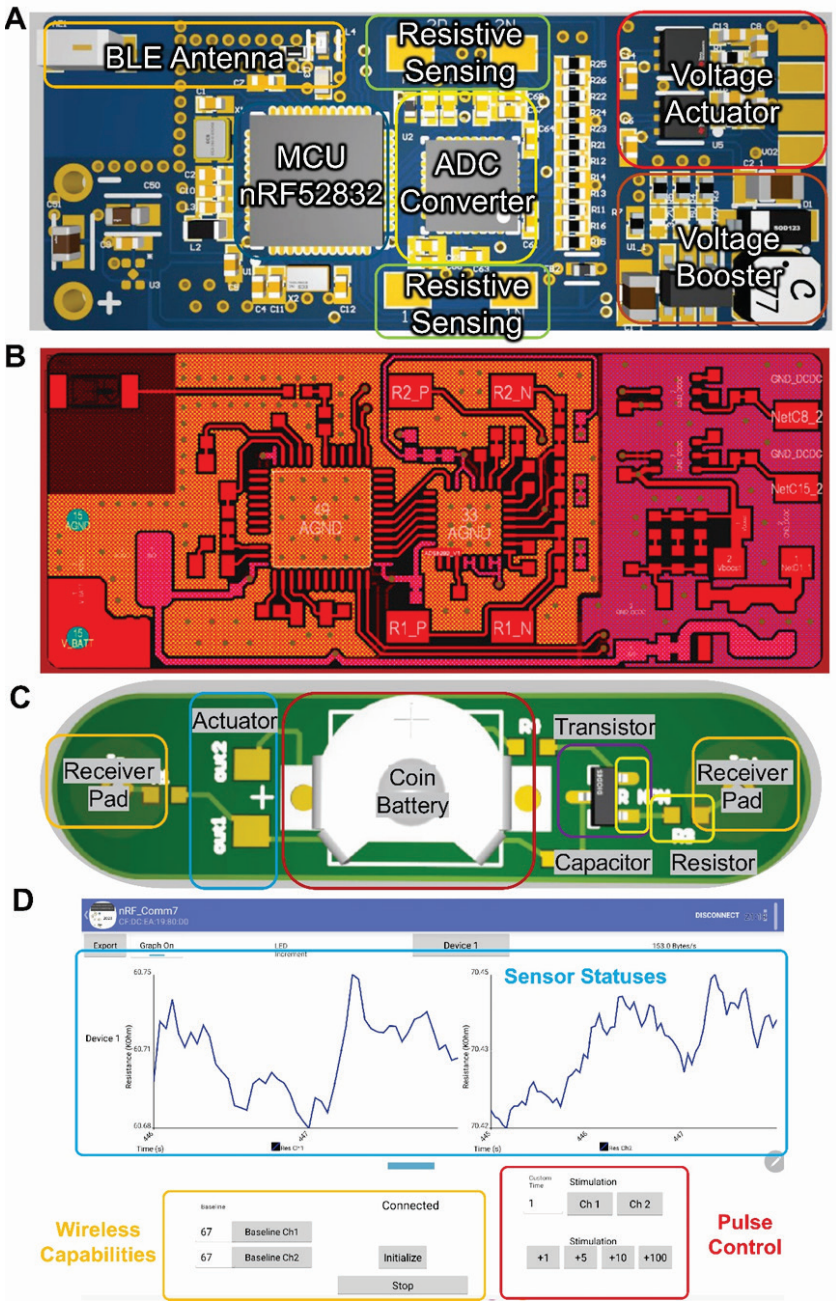

SI 6. **Multiplexed wireless sensing utilizing serpentine traces and laser-induced graphene sensors.** (A) Fabrication of a uniaxial laser-induced graphene (LIG) sensor; Al = aluminum, PDMS = polydimethylsiloxane, Cu = copper, PI = polyimide, SEBS = styrene-ethylene-butylene-styrene block co-polymer. (B) Fabrication of bilayer copper-polyimide serpentine traces. (C) Fabrication of bilayer copper-polyimide interconnect. (D) Strain-resistance calibration curve of 8 LIG sensors (individual = gray lines, average = black line).

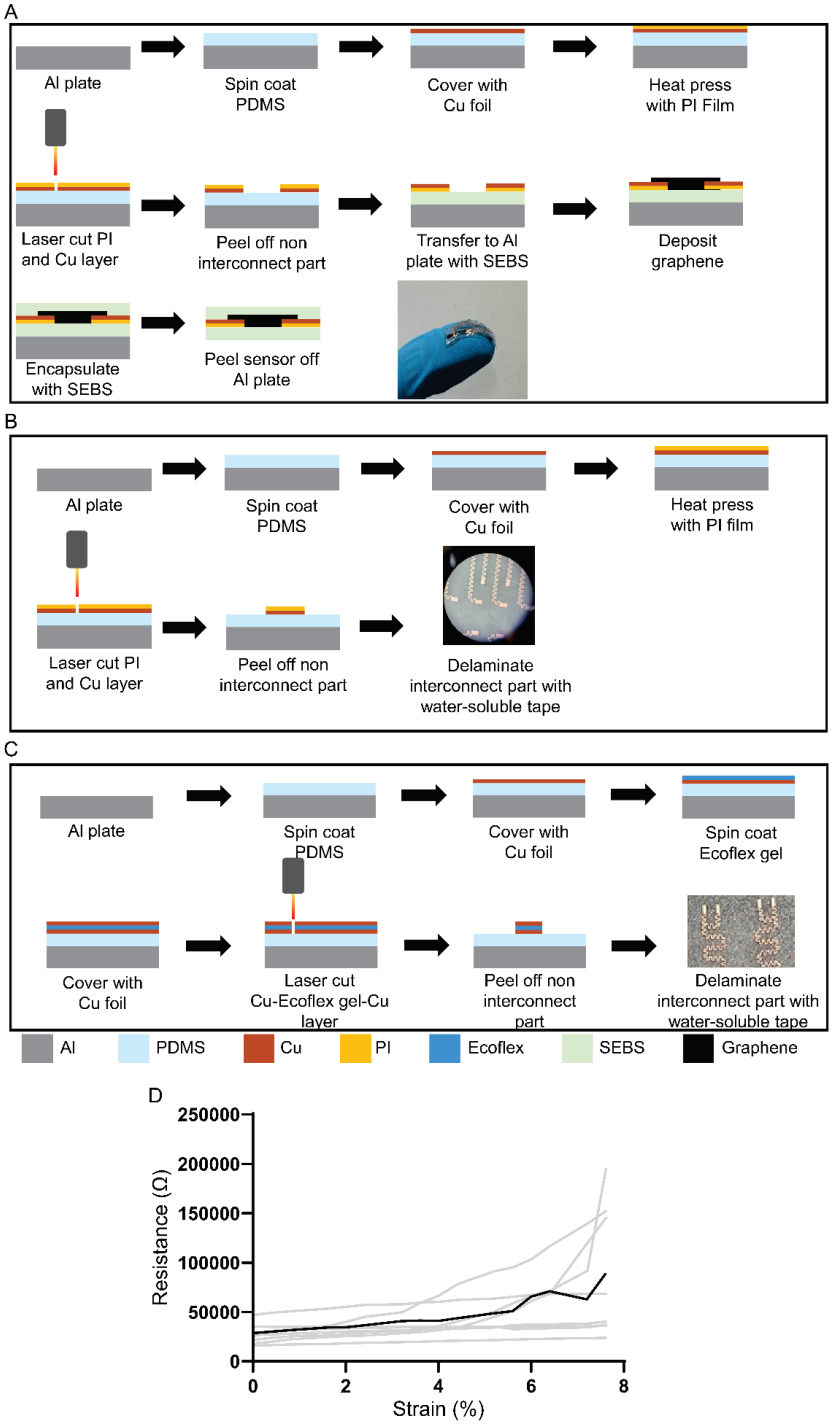
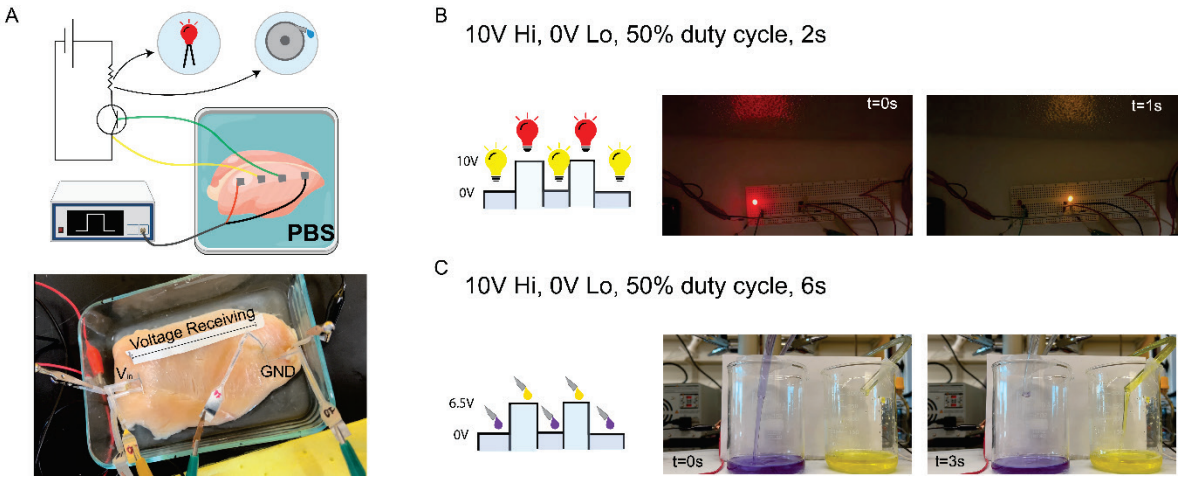
SI 7. Integrating various actuators for communication via IBC ex vivo. (A) Ex vivo set up for switching on various electromechanical devices including an LED and a pump. The gate pins of the transistor are connected to tissue-interfacing receiving pads. The electromechanical device is illustrated as a resistive load in the schematic. (B) Utilizing a PNP and an NPN along with a [10 V, 0 V, 1 s] pulse allows for selective triggering of 2 LEDs. (C) Utilizing a PNP and a MOSFET along with a [6.5 V ,0 V, 3 s] pulse allows for selective triggering of 2 pumps.